



Tidal Disruptions of Stars by Binary Black Holes: Modifying the Spin Magnitudes and Directions of LIGO Sources in Dense Stellar Environments

Martin Lopez, Jr.^{1,2} , Aldo Batta^{1,2,3} , Enrico Ramirez-Ruiz^{1,2} , Irvin Martinez^{2,4}, and Johan Samsing⁵

¹ Department of Astronomy and Astrophysics, University of California, Santa Cruz, CA 95064, USA

² Niels Bohr Institute, University of Copenhagen, Blegdamsvej 17, DK-2100 Copenhagen, Denmark

³ Instituto Nacional de Astrofísica, Óptica y Electrónica, Tonantzintla, Puebla 72840, México

⁴ Departamento de Física, Universidad de Guanajuato—DCI, C.P. 37150, León, Guanajuato, México

⁵ Department of Physics & Astronomy, Princeton University, Princeton, NJ 08544, USA

Received 2018 December 3; revised 2019 April 4; accepted 2019 April 9; published 2019 May 24

Abstract

Binary black holes (BBHs) appear to be widespread and are able to merge through the emission of gravitational waves, as recently illustrated by Laser Interferometer Gravitational-Wave Observatory (LIGO). The spin of the BBHs is one of the parameters that LIGO can infer from the gravitational-wave signal and can be used to constrain their production site. If BBHs are assembled in stellar clusters, they are likely to interact with stars, which could occasionally lead to a tidal disruption event (TDE). When a BBH tidally disrupts a star, it can accrete a significant fraction of the debris, effectively altering the spins of the BHs. Therefore, although dynamically formed BBHs are expected to have random spin orientations, tidal stellar interactions can alter their birth spins both in direction and magnitude. Here we investigate how TDEs by BBHs can affect the properties of the BH members as well as exploring the characteristics of the resulting electromagnetic signatures. We conduct hydrodynamic simulations with a Lagrangian Smoothed Particle Hydrodynamics code of a wide range of representative tidal interactions. We find that both spin magnitude and orientation can be altered and temporarily aligned or anti-aligned through accretion of stellar debris, with a significant dependence on the mass ratio of the disrupted star and the BBH members. These tidal interactions feed material to the BBH at very high accretion rates, with the potential to launch a relativistic jet. The corresponding beamed emission is a beacon to an otherwise quiescent BBH.

Key words: binaries: close – globular clusters: general – gravitational waves – stars: black holes

1. Introduction

A watershed event occurred on 2015 September 14, when the Laser Interferometer Gravitational-Wave Observatory (LIGO) succeeded in detecting the first gravitational-wave (GW) signal (Abbott et al. 2016), GW150914, of a binary black hole (BBH) merger. This detection was followed by nine others (The LIGO Scientific Collaboration & The Virgo Collaboration 2018), which have unveiled a population of stellar mass BHs that is significantly heavier than those inhabiting X-ray binaries (Farr et al. 2011).

A large number of progenitor systems have been suggested, all designed to manufacture BHs in the observed mass range. The two most widely discussed scenarios encompass dynamical assembly in dense star clusters (Sigurdsson & Hernquist 1993; Portegies Zwart & McMillan 2000; Downing et al. 2010, 2011; Samsing et al. 2014, 2018a; Ziosi et al. 2014; Rodriguez et al. 2015, 2016b, 2016c; Samsing & Ramirez-Ruiz 2017) and isolated massive stellar field binaries (Paczynski 1976; Iben & Livio 1993; Podsiadlowski 2001; Voss & Tauris 2003; Kalogera et al. 2007; Taam & Ricker 2010; Dominik et al. 2012, 2013; Ivanova et al. 2013; Postnov & Yungelson 2014; Belczynski et al. 2016; Schröder et al. 2018), including chemically homogeneous stars (de Mink et al. 2009; de Mink & Mandel 2016; Mandel & de Mink 2016; Marchant et al. 2016).

Other proposed scenarios include active galactic nuclei disks (Bartos et al. 2017; Stone et al. 2017; McKernan et al. 2018), galactic nuclei (O’Leary et al. 2009; Hong & Lee 2015; Antonini & Rasio 2016; Stephan et al. 2016; VanLandingham et al. 2016; Hoang et al. 2018), single-single GW captures of primordial BHs (Bird et al. 2016; Carr et al. 2016; Cholis et al. 2016;

Sasaki et al. 2016; Askar et al. 2017), and very massive stellar mergers (Loeb 2016; Woosley 2016; Janiuk et al. 2017; D’Orazio & Loeb 2018). Generally, these theoretical predicted channels can be broadly tuned to be consistent with the properties and rates of the BBH sources observed by LIGO so far, and the challenge remains to find reliable observational tests.

Recent work suggests that the key parameters that might help discriminate between formation channels include the BH mass (e.g., Zevin et al. 2017), orbital eccentricity in LIGO (O’Leary et al. 2009, 2016; Kocsis & Levin 2012; Samsing et al. 2014, 2018a, 2018b; Samsing & Ramirez-Ruiz 2017; Gondán et al. 2018; Rodriguez et al. 2018a; Samsing 2018; Samsing & Ilan 2018, 2019; Zevin et al. 2019) and LISA (e.g., Samsing & D’Orazio 2018), and especially the dimensionless spin parameter χ_{eff} (Rodriguez et al. 2016c; Farr et al. 2017, 2018; Schröder et al. 2018). χ_{eff} is the total mass weighted BH spin components in the direction of the orbital angular momentum,

$$\chi_{\text{eff}} = \frac{M_{\text{bh}_1} S_{\text{bh}_1} + M_{\text{bh}_2} S_{\text{bh}_2}}{M_{\text{bh}_1} + M_{\text{bh}_2}} \cdot \hat{\mathbf{L}}. \quad (1)$$

Here S_{bh_1} and S_{bh_2} are the dimensionless spins of the BHs, and $\hat{\mathbf{L}}$ is the direction of the orbital angular momentum. The spin measurements of BBHs arising from the isolated massive stellar field binary scenario roughly predict the alignment of the BH spins and the orbital angular momentum (Kalogera 2000), while dynamically assembled BHs are expected to have uncorrelated spins as they are formed and harden through a series of chaotic exchange interactions (Rodriguez et al. 2016c).

Here we will analyze the dynamical scenario and investigate whether the determination of χ_{eff} allows for constraints to be placed on the spin history of the BBH system between assembly and merger. The most telling observations of BBHs come from dense star clusters, where stars are crowded close enough to each other to undergo frequent interactions. Such a BBH becomes detectable only through interactions with its gaseous environment. Gas that is lost from nearby stars, or even stars plunging into such binaries, can produce detectable signatures as well as alter the spins of the BH members. It is the interplay between BBHs and stars in a dense environment that may allow us to use GWs and electromagnetic observations to draw firm conclusions about their assembly history. Through the use of Smoothed Particle Hydrodynamic (SPH) simulations, we show how stellar material that is accreted following a tidal disruption event (TDE) can potentially alter the birth spin magnitudes and orientations of the individual BHs, possibly aligning or misaligning them temporarily. Furthermore, the supply of material to the BBH is above the Eddington limit and could launch a relativistically beamed jet. The emerging class of high-energy transient bursts all have peak luminosities and durations reminiscent of ultra-long γ -ray bursts. Tidal disruptions of stars by BBHs thus uniquely probe the currently debated existence of LIGO signals emanating from dense star clusters.

The structure of the paper is as follows. Section 2 discusses the dynamics of LIGO BBH (LBBH) TDEs in dense star clusters. Section 3 overviews the hydrodynamic formalism and presents the results as well as their significance for the spin magnitude and alignment of the individual BHs. Section 4 explores the implications of our results and possible sources for upcoming high-energy transient surveys.

2. TDEs by LIGO BBHs

2.1. Single BH Dynamics

Canonical TDEs occur when a star with mass M_* and radius R_* gets disrupted when approaching a supermassive black hole (SMBH) with mass M_{bh} at a pericenter distance $R_p = R_\tau = q^{-1/3}R_*$, where $q = M_*/M_{\text{bh}}$ (Rees 1988; Evans & Kochanek 1989; Phinney 1989). After the disruption, about half of the star becomes unbound and ejected, while the other half becomes bound to the SMBH on elliptical orbits. Three-dimensional (3D) hydrodynamical simulations have quantified the rate at which material falls back onto the SMBH (Guillochon & Ramirez-Ruiz 2013). A good fit to the observed light curves of TDEs is obtained if one assumes that the accretion luminosity directly follows the fallback rate in the simulation (Mockler et al. 2019). However, it is not clear why this should be the case. Bound debris returns to the SMBH with a large range of eccentricities and orbital periods (Ramirez-Ruiz & Rosswog 2009) and it may take many Keplerian orbits for fallback material to circularize and accrete (Guillochon & Ramirez-Ruiz 2015). Some mechanism is therefore required to quickly dissipate the kinetic energy of the fallback material and circularize it into an accretion disk.

In standard TDE discourse (Rees 1988), the disrupting SMBHs have masses $M_{\text{bh}} \gtrsim 10^6 M_\odot$ yielding $q \ll 1$, which allows the semimajor axis of the most bound material to be

approximated as

$$a_{\text{mb}} = \left(\frac{M_{\text{bh}}}{M_*} \right)^{1/3} R_\tau \\ = q^{-1/3} R_\tau. \quad (2)$$

However, for disrupting BHs within an LBBH, the mass ratio is near unity, making the extent of the star comparable to the tidal radius. In this case, the specific orbital energy of stellar material varies significantly across the star. In a reference frame where the disrupting BH is positioned at the origin such that the star's center of mass (CM) is located at a distance $r' = R_\tau$, the stellar material has energy $E(r')$. We transform to the CM reference frame of the star and the energy of stellar material can be calculated as $E(r)$, where r is the distance from the star's CM. In this case,

$$E(r) = E(r' = R_\tau - r) - E(r' = R_\tau) \\ = -GM_{\text{bh}} \left[\sum_{n=1}^{\infty} \left(\frac{q^{1/3}}{R_*} \right)^{n+1} r^n \right]. \quad (3)$$

For material that is bound to the BH, this expression translates into a range of semimajor axes given by

$$a(r) = -\frac{GM_{\text{bh}}}{2E(r)} \\ = \left[2 \sum_{n=1}^{\infty} \left(\frac{q^{1/3}}{R_*} \right)^{n+1} r^n \right]^{-1}, \quad (4)$$

which for canonical TDEs ($q \ll 1$) can be safely approximated to first order to give Equation (2) by plugging in $r = R_*$, where the factor of 2 difference is due to the fact that Equation (2) is using the *average* specific binding energy. As q approaches unity, this approximation is no longer valid, and the semimajor axis of the most bound material approaches the tidal radius and becomes equal to it at a critical mass ratio $q_{\text{crit}} = 0.037$. The assumption that the circularization radius of the most bound material is about twice the tidal radius (Cannizzo et al. 1990; Ulmer 1998; Gezari et al. 2009; Lodato & Rossi 2011; Strubbe & Quataert 2011; Guillochon et al. 2014) also breaks down in the LBBH regime. The circularization radius of the most bound material $R_{c,\text{mb}}$ in this case is given by

$$R_{c,\text{mb}} = 2R_\tau [1 - q^{1/3}]^2, \quad (5)$$

while the spread in circularization radii can be written as

$$\frac{\Delta R_c}{R_{c,p}} = q^{1/3} [2 - q^{1/3}], \quad (6)$$

where the circularization radius of the pericenter is $R_{c,p} = 2R_\tau$. In order for this material to circularize and form a disk, energy must be dissipated efficiently after disruption. Material falling to pericenter can be heated by hydrodynamical shocks, and Guillochon et al. (2014) show that the fractional energy dissipation per orbit, ν_H , can be written as

$$\nu_H = \beta q^{2/3}, \quad (7)$$

where $\beta = R_p/R_\tau$. For disruptions in the LBBH regime, the energy dissipation via shocks at pericenter can be sizable and lead to efficient circularization. This is in contrast to the

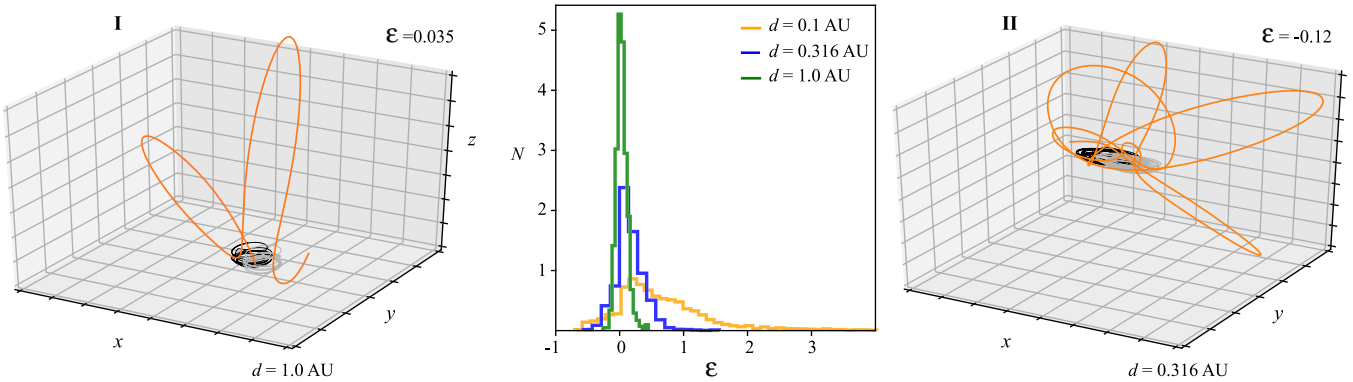


Figure 1. The CM energy distributions with respect to the disrupting BH and specific trajectories are shown for a Sun-like star ($M_* = 1M_\odot$, $R_* = R_\odot$) interacting with a $15M_\odot$ equal mass BH binary with $e = 0.5$. The properties of the binary have been selected to reflect those derived by Rodriguez et al. (2016a) for dynamically assembled LBBHs. Here we study the outcomes of TDE interactions and their associated CM energy distributions by performing a large set of numerical scattering experiments using the N -body code developed by Samsing et al. (2014). The panels shows the energy distribution for different binary separations ($d = 1.0$ au = $87.3R_\tau$, $d = 0.316$ au = $27.6R_\tau$, $d = 0.1$ au = $8.73R_\tau$) and the trajectories of unbound (I) and bound (II) stellar orbits (orange trajectories). Here ε is the CM energy of the star with respect to the disrupting BH at R_τ in units of the binding energy of the star.

standard case with $q \ll 1$, for which hydrodynamical shocks at pericenter are likely to be insufficient and rapid circularization might only be achieved via general relativistic effects (Guillochon & Ramirez-Ruiz 2015; Shiokawa et al. 2015; Bonnerot et al. 2016; Hayasaki et al. 2016). We note here that not all the binaries we refer to as LBBH will necessarily merge.

2.2. Binary BH Dynamics

For BBH TDEs, the star does not necessarily follow a parabolic orbit and the orbital deviations before disruption depend strongly on the separation d , identified here as the semimajor axis, and eccentricity e of the binary. The CM energy distributions of a Sun-like star with respect to the disrupting BH part of a $15M_\odot$ equal mass BBH with $e = 0.5$ are shown in Figure 1 for three distinct binary separations. The plotted outcomes are derived by performing a large set of numerical scattering experiments using the N -body code developed by Samsing et al. (2014). The trajectory of the star is halted when the pericenter distance closely approaches the tidal radius. In this case, $R_\tau = 2.47R_\star = 0.01$ au. The selected properties of the BBHs (eccentricity, masses, and separation) are chosen to match those derived by Rodriguez et al. (2016a). The type of star that is disrupted is highly sensitive to the evolutionary state of the cluster at the time when most of these encounters are expected to occur (Breen & Heggie 2013; Arca Sedda et al. 2018; Askar et al. 2018). Here we have selected a Sun-like star in order to facilitate comparison with previous TDE calculations. We will nevertheless return to discuss this critical issue in subsequent sections.

For $R_\tau/d \ll 1$, the CM energy is essentially parabolic while a larger fraction of unbound CM orbits are observed for tighter binaries. This is partly due to the individual BHs evolving faster around their binary CM as BBHs get tighter, which then maps to a higher relative velocity at the time of disruption and thereby a higher relative energy. Note here that stellar elements unbound with respect to the disrupting BH can still be bound to the CM of the BBH, which then can lead to later accretion.

After disruption, the fate of the debris also depends sensitively on the ratio R_τ/d . If $R_\tau/d > 1$, the disruption will take place outside of the binary and the infalling material will form a circumbinary disk around the system. In what follows, we refer to

this scenario as the *circumbinary scenario* (CS). When $R_\tau/d \lesssim 1$, the star will be disrupted by one of the binary members but the accretion history of the debris onto the system is determined by d . This is due to the debris orbiting around the disrupting BH with a wide range of semimajor axes such that there is always some material that is able to reach the sphere of influence of the companion BH. In order to determine whether or not the non-disrupting BH can accrete significant amounts of stellar debris, we make use of two important characteristic length scales. One is the semimajor axis a_{90} of the disrupted material whose orbit contains 90% of the stellar debris. The stellar radius corresponding to such material is R_{90} , which can be obtained by integrating mass from the edge of the star closest to the disrupting BH (i.e., the most bound material) toward the stellar core until the accumulated mass is $0.9M_*$. Once R_{90} is obtained, we can use Equation (4) to calculate the semimajor axis associated with such an orbit. Therefore, we classify a strong interaction as being one where the non-disrupting BH interacts with at least 10% of stellar debris. The other scale is the Roche lobe radius R_L , which determines the gravitational sphere of influence of the disrupting BH. R_L can be written (Eggleton 1983) as

$$\frac{R_L}{d_{\min}} = \frac{0.49q_b^{2/3}}{0.6q_b^{2/3} + \ln(1 + q_b^{1/3})}, \quad (8)$$

where q_b is the mass ratio of the BBH and d_{\min} is the minimum separation of the binary. When $a_{90}/R_L < 1$, a small fraction of the debris is able to interact with the non-disrupting BH but most of the stellar debris will be accreted by the disrupting BH. In this case, the tidal interaction will resemble that caused by a single BH, and we refer to this as the *single scenario* (SS). On the other hand, disrupted material with $a_{90}/R_L \gtrsim 1$ will be influenced by the companion and a sizable fraction of debris can be accreted by the non-disrupting BH; a case we refer to as the *overflow scenario* (OS).

In order to calculate the change of spin due to accretion of disrupted material in units of the maximal BH spin, we use (Bardeen 1970)

$$S(M_{bh,f}) = \left(\frac{2}{3}\right)^{1/2} \frac{M_{bh}}{M_{bh,f}} \left\{ 4 - \left[18 \left(\frac{M_{bh}}{M_{bh,f}} \right)^2 - 2 \right]^{1/2} \right\}, \quad (9)$$

which assumes an initially low or non-spinning BH. Here $M_{\text{bh,f}} = M_{\text{bh}} + fM_{\star}$ is the final mass of the BH after accreting a fraction f of the disrupted star. For a TDE of a star in a parabolic orbit ($f = 0.5$), the maximum mass that the BH can accrete is $0.5M_{\star}$ such that the maximum spin up, S_{\max} is given by

$$S_{\max}(q) = \left(\frac{8}{3}\right)^{1/2} \left(\frac{1}{2+q}\right) \left\{ 4 - \left[72 \left(\frac{1}{2+q}\right)^2 - 2 \right]^{1/2} \right\}, \quad (10)$$

The values of S_{\max} for a few characteristic q 's are $S_{\max}(q = 1 \times 10^{-6}) = 1.84 \times 10^{-6}$, $S_{\max}(q = 0.01) = 0.02$, and $S_{\max}(q = 0.5) = 0.60$. This clearly illustrates that for LBBHs, the digestion of stars during the lifetime of the binary could lead to noticeable spin changes.

3. Hydrodynamics

3.1. Setup

Our hydrodynamical simulations of LBBH TDEs use modified versions of the SPH code GADGET (Springel 2005; Pakmor et al. 2012). GADGET allows one to accurately follow the accretion of material into sink particles and the compressibility of the gas is described with a gamma-law equation of state $P \propto \rho^{\gamma}$. By solving the Lane–Emden equation and using the same method as in Batta et al. (2017), we created 3D spherically symmetric distributions of SPH particles by mapping polytropic stars in hydrodynamical equilibrium with a structural gamma Γ set to either 5/3 or 4/3, representative of low- and high-mass stars, respectively. During the simulation, the stars are evolved hydrodynamically according to a $\gamma = 5/3$ equation of state, with the difference between Γ and γ for higher-mass (or convective) stars being a consequence of radiation transfer in the star's interior. We ran test cases of the tidal disruption of a $1M_{\odot}$ star by an equal mass $M_{\text{bh}_1} = M_{\text{bh}_2} = 15M_{\odot}$ LBBH with varying resolutions between $N = 10^5$ and 10^6 particles, which showed clear convergence for the accretion rates and mass bound to the system.

3.2. Initial Conditions (ICs)

All ICs assume typical parameters for LBBHs (Rodriguez et al. 2016a) and stars (Kroupa et al. 2013) in globular clusters (GCs). We take $e = 0.5$ for the LBBH's eccentricity and assume that the individual spins of the BHs (S_1 and S_2) are initially zero, which is consistent with the small spins observed for LIGO events so far (The LIGO Scientific Collaboration & The Virgo Collaboration 2018). The mass of the disrupted star is critical. This is because the change in the spins of LBBHs experiencing a TDE depends heavily on q , as shown in Equation (10). Interactions with heavier stars are expected to take place early in the evolution of the cluster while disruptions of low mass stars will be more prevalent in older clusters (Breen & Heggie 2013; Arca Sedda et al. 2018; Askar et al. 2018). An encounter with a modestly massive star is expected to have a sizable effect on the spin and might occur more frequently early in the evolution of clusters when the number density of BBHs is expected to be higher (Kremer et al. 2019). Motivated by this, we contrast here the results from the disruption of a Sun-like star with those arising from the disruption of a $5M_{\odot}$ star. In addition, we select various stellar

radii of the disrupted stars to match the properties of a solar-like star, a massive main-sequence (MS) star, and a slightly evolved Sun-like star.

By means of a three-body code, we obtained the dynamical properties of the LBBH and star prior to a tidal disruption, tracing the trajectories for all three bodies back in time when the incoming star lies about six tidal radii away from the disrupting BH. The initial angle of the trajectory with respect to the LBBH orbital plane was chosen arbitrarily by virtue of this angle being isotropically distributed (see Section 4.1.1 for more details). The impact parameter for these trajectories is approximately R_{τ} of the respective simulation, otherwise there would be a negligible or non-interaction between the star and LBBH. These dynamical properties were included in the GADGET IC file.

3.3. Simulation Results

In Section 2.2, we have outlined three representative scenarios for LBBH TDEs: SS, CS, and OS. In the SS case, we have $R_{\tau} \ll d$ and $a_{90} < R_L$ and the event resembles that from a single BH TDE in which only one BH accretes. In the CS case, we have $R_{\tau} > d$ and the LBBH ends up being embedded in a circumbinary disk. In the OS case, we have $R_{\tau} \lesssim d$ and $a_{90} > R_L$ and the accretion of the disrupted debris by both BHs is able to produce multiple TDEs. The simulation results for the various cases outlined here are presented in Sections 3.3.1–3.3.4 and shown in Figures 2 and 3.

3.3.1. The Single Scenario

The SS simulation is characterized here by $R_{\tau}/d = 0.006$ and $a_{90}/R_L = 0.54$. For these ICs, almost no significant interaction of the disrupted material is expected to occur with the non-disrupting BH. The SS simulation shown here is consistent with the scenario shown in Figure 1 for an unbound stellar orbit. The *top panels* in Figure 2 show the gas column density in the orbital plane at three different times, which are shown in units of the dynamical timescale of the star defined as $t_* = (R^3/GM)^{1/2}$. The bound material is observed to circularize promptly and, as a result, the mass accretion rate is observed to follow the standard mass fallback rate. However, given that $q = 0.066$, the early shape of the mass accretion rate curve differs from that derived by Guillochon & Ramirez-Ruiz (2013), which was calculated assuming $q \ll 1$. By the end of the simulation, the disrupting BH accreted a total mass of $0.1M_{\odot}$ and has an accretion disk with a leftover mass of about $0.12M_{\odot}$ and whose angular momentum \mathbf{J}_{disk} is inclined about 1.75 rad with respect to the orbital angular momentum of the binary \mathbf{J}_{bin} . This angle is consistent with that of the star's angular momentum at the moment of disruption. Assuming that the bound $\approx 0.12M_{\odot}$ of material is accreted by the BH, the resultant spin magnitude will be $S_1 \approx 0.05$, resulting in an anti-aligned effective spin of $\chi_{\text{eff}} \approx -0.045$.

3.3.2. The Circumbinary Scenario

The CS simulation is parameterized by $R_{\tau}/d = 2.47$. The tidal radii of each BH overlap and encompass the binary, resulting in a disruption where bound material forms a circumbinary disk. At the moment of disruption, the orientation of the angular momentum of the star's CM with respect to \mathbf{J}_{bin} is approximately 2.44 rad. As the most bound material returns

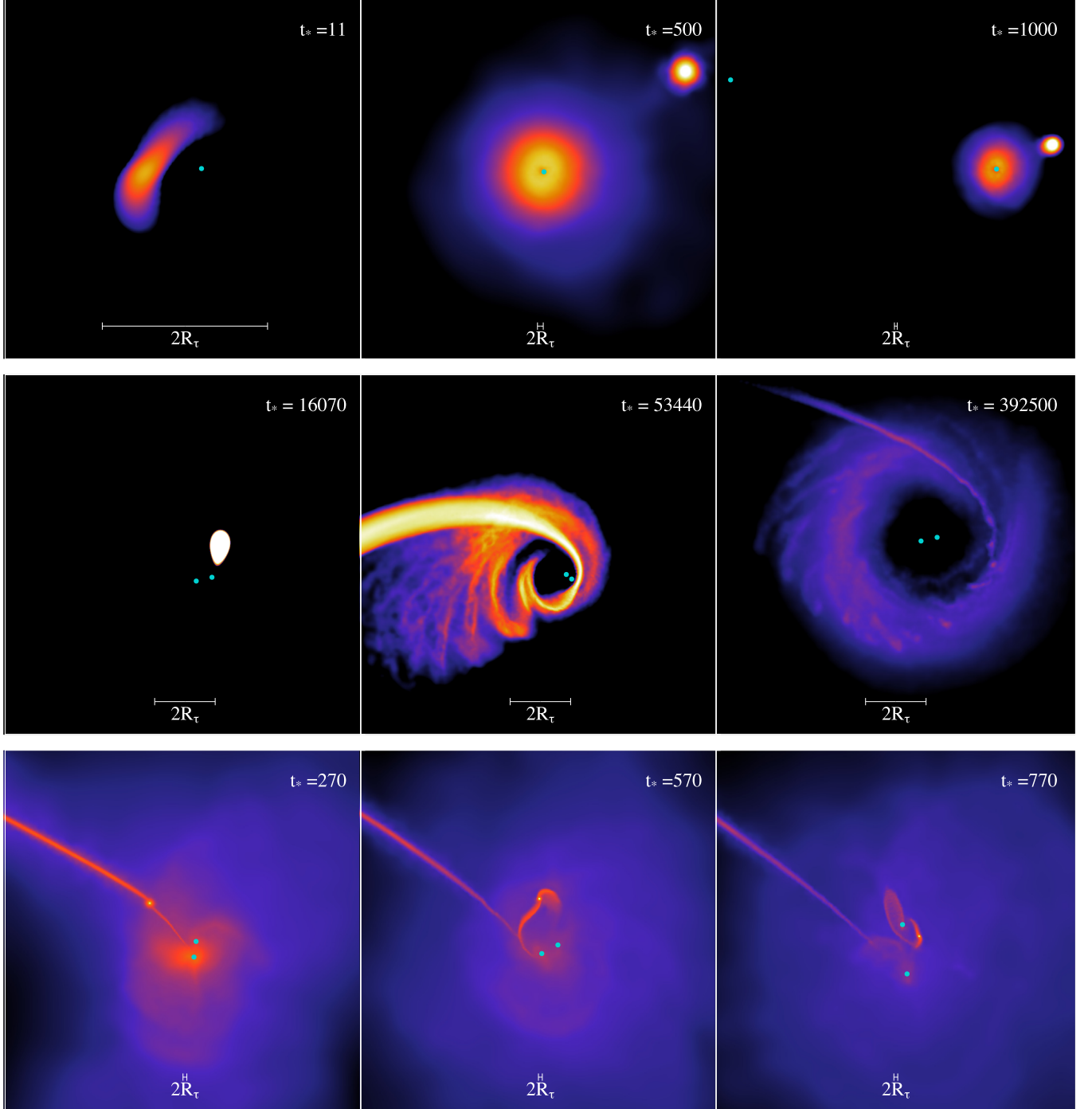


Figure 2. Simulations of the tidal interaction of stars with an LBBH. Here t_* and R_τ are the simulation times in the star’s dynamical timescale and the corresponding tidal radii. All panels are in the orbital plane of the LBBH. Top panels: simulation of the SS case at three different times, from disruption to the subsequent accretion onto the disrupting BH. Middle panels: simulation of the CS case at three different times, from the initial disruption occurring outside the LBBH to the assembly of the circumbinary disk. Bottom panels: simulation of the OS case, from initial partial disruption of the star, followed by a second and third disruption of the remaining stellar core. During this interaction, a total of four disruptions occur. The simulation parameters, listed as [SS, CS, OS], are: $N = [10^5, 10^6, 10^5]$, $R_* = [1, 43, 1]R_\odot$, $\Gamma = [4/3, 5/3, 4/3]$, $d = [429.88, 42.99, 42.99]R_\odot$, $v_\infty = [30, 10, 20] \text{ km s}^{-1}$. In all cases $M_* = 1M_\odot$, $M_{\text{bh1}} = M_{\text{bh2}} = 15M_\odot$, and $e = 0.5$.

to pericenter, the binary exerts a torque on the stream and, as a result, alters the angle of \mathbf{J}_{disk} to ≈ 2 rad; see Section 4.1 and Figure 5. The disk rapidly circularizes due to hydrodynamical dissipation at pericenter as well as collisions between the returning stream caused by the time changing binary potential (*middle panels* in Figure 2). The material residing in the disk is slowly accreted onto both BHs through viscous dissipation. We

stopped the simulation at approximately 10% of the time it would take to ingest the entire disk and found that each BH accreted about $0.01M_\odot$ and the accretion disk has $0.3M_\odot$ of gas leftover. If we assume that this material is evenly accreted by both BHs, the resultant spin magnitudes will be $S_1 = S_2 \approx 0.036$ and, given that the spin angles of each BH are aligned with \mathbf{J}_{disk} , $\chi_{\text{eff}} \approx -0.015$.

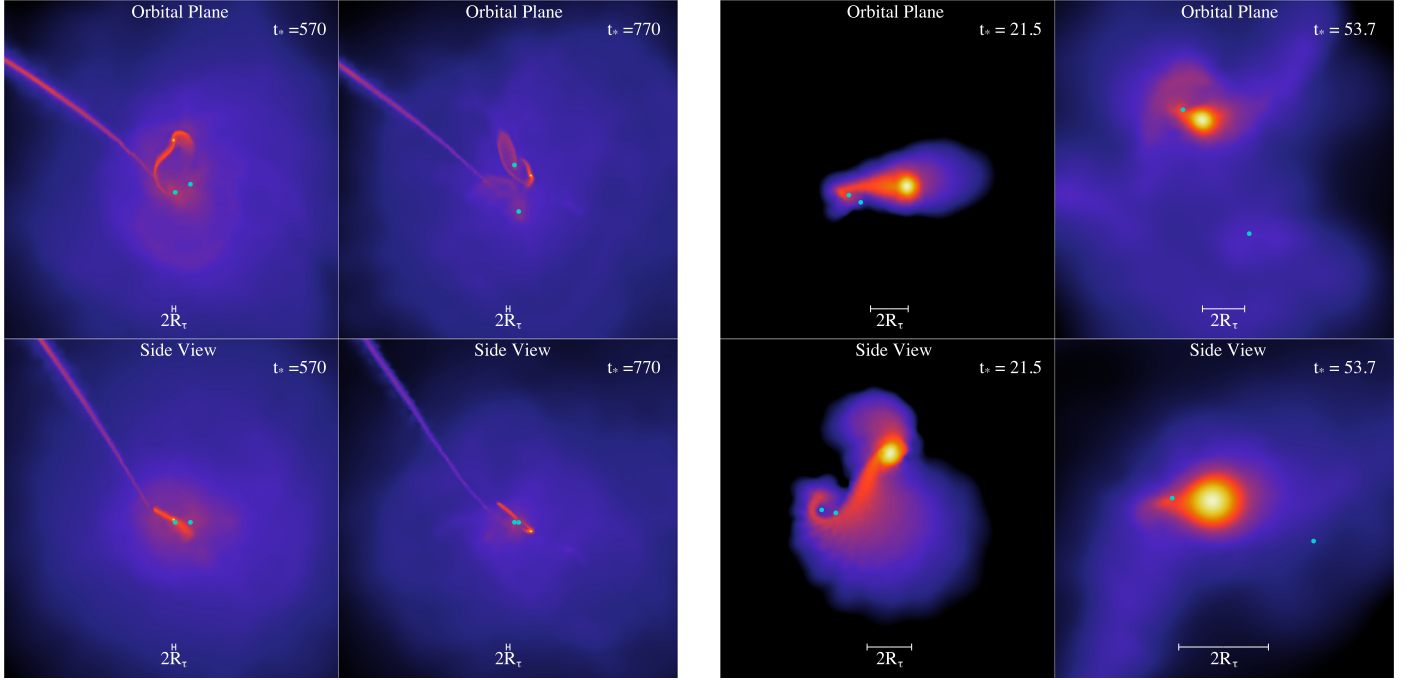


Figure 3. A comparison between two OS simulations. Here t_* denotes the time in units of the star’s dynamical timescale while R_τ shows the scale of the individual BH tidal radius. Left panel: here we show the simulation snapshots for the OS shown in Figure 2. The additional side views plotted here clearly show how the orientation of the accretion disk changes between the multiple disruptions. Right panel: shown are the simulation snapshots for the MOS discussed in Section 3.3.4. The orbital view shows the two interactions that take place until full disruption of the star. In the side view snapshots one can clearly see that the orbital angular momentum of the binary is altered by the three-body interaction. This change is significant in this case due to the higher mass ratio between the star and the BBH. The simulation parameters for the MOS are: $N = 10^5$, $M_* = 5 M_\odot$, $R_* = 6 R_\odot$, $\Gamma = 4/3$, $M_{\text{bh1}} = M_{\text{bh2}} = 10 M_\odot$, $d = 21.49 R_\odot$, $v_\infty = 30 \text{ km s}^{-1}$, $e = 0.5$.

3.3.3. The Overflow Scenario

The OS simulation is characterized here by $R_\tau/d = 0.06$ and $a_{90}/R_L = 5.44$. This guarantees that after the disruption, a significant amount of bound disrupted material will be able to reach the sphere of influence of the non-disrupting BH. Within this scenario, accretion onto both BHs can occur, which might result in temporary BH spin alignment or anti-alignment. The star survives after the initial disruption leading to multiple resonant TDEs, as can be seen in the bottom panels of Figure 2. A total of four interactions take place with the same BH in this scenario until the star is fully disrupted. The angular momentum of the star with respect to \mathbf{J}_{bin} changes in each disruption. By the end of the simulation, the mass accreted by the disrupting and non-disrupting BHs is $0.19 M_\odot$ and $0.02 M_\odot$, respectively. The resultant angles are 1.58 rad and 0.24 rad with respect to \mathbf{J}_{bin} for the disrupting and non-disrupting BHs, respectively. The first disruption provides the majority of the accreted mass for the disrupting BH, while the non-disrupting BH accretes mass as it returns to the pericenter of the binary orbit. Therefore, the angle for the disrupting BH is similar to that of the star’s angular momentum with respect to \mathbf{J}_{bin} at the time of the first disruption, while the non-disrupting BH’s angle is aligned with \mathbf{J}_{bin} ; see Section 4.1 and Figure 5. We obtain $S_1 \approx 0.04$ and $S_2 \approx 0.006$ which leads to a final $\chi_{\text{eff}} \approx 0.003$.

3.3.4. The Massive Overflow Scenario (MOS)

The changes in spin magnitude obtained in the scenarios discussed previously are expected to be small given that $S_{\max}(q = 0.067) = 0.12$. More sizable changes are expected

for larger values of q . Motivated by this, we run a simulation in which $q = 0.5$, which we refer to as the MOS. The MOS simulation is characterized by $R_\tau/d = 0.35$ and $a_{90}/R_L = 16.14$. A comparison between the OS and MOS is shown in Figure 3.

Both OS and MOS simulations lead to multiple disruptions and result in accretion onto both BHs. However, the \dot{M} curves shown in Figure 4 are significantly different. In the OS, accretion onto the disrupting BH proceeds like in canonical TDEs, showing a fast rise and a subsequent power-law decay. Accretion onto the non-disrupting BH, which occurs as it plummets into the accretion disk around the disrupting BH, is observed to be delayed and increases at a slower rate. In the MOS panel, accretion onto both BHs occurs at a similar time, and the \dot{M} curves for both BHs are rather similar yet differ from the canonical TDEs. In this case, the first disruption was weaker and most of the material was made available to the BHs until after the second disruption (Figure 4). The star gets considerably closer to the BH during the second encounter and, as a result, the star is completely disrupted. In what follows, we refer to the disrupting BH as the one responsible for the second disruption, which provides the vast majority of the mass supply. The accretion disk that forms after the second disruption can be seen in the right bottom panel of Figure 4 and is observed to be very extended, making it easy for the non-disrupting BH to accrete a substantial amount of material, especially since the binary orbit is highly eccentric and the BH will eventually plunge into the accretion disk.

The mass accreted by the disrupting and non-disrupting BH at the end of the simulation is $0.91 M_\odot$ and $0.40 M_\odot$, respectively. This leads to $S_1 \approx 0.283$ at angle 2.2 rad with

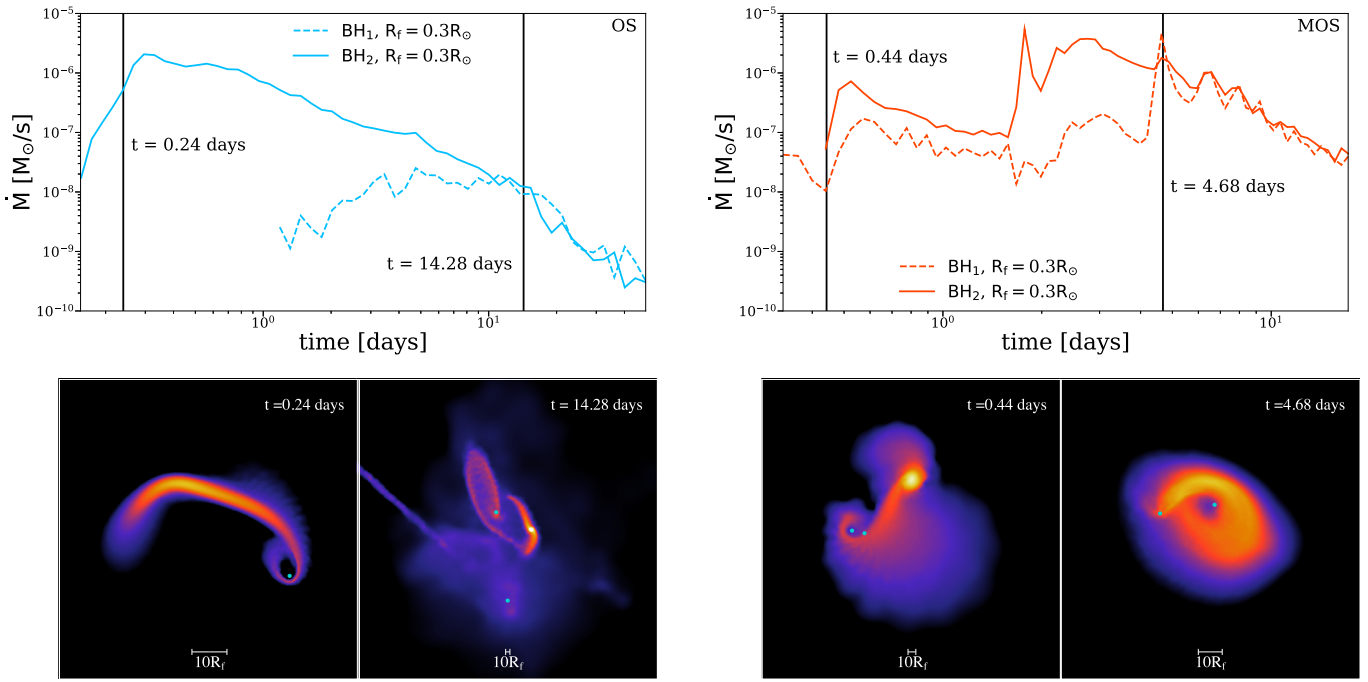


Figure 4. The mass accretion histories experienced by both BHs in the OS and MOS. Here R_f is the *Fallback Radius* of the surface at which the mass flux is calculated. All snapshot times are measured from the time the most bound material is accreted. Left panel: the top panel shows accretion curves for both BHs for the OS. A total of four tidal interactions take place. The first is responsible for feeding significant mass to the disrupting, while the non-disrupting BH accretes material as it plunges into the disk around the disrupting BH. The bottom panels show snapshots of the simulation at 0.24 and 14.3 days (shown as vertical lines in the top panel). Right panel: the top panel shows the rate of mass accretion onto both BHs. In contrast to the OS, both BHs accrete promptly due to the larger amount of stellar material available. After the second disruption the accretion curves are almost identical. In this case, both BHs accrete a notable percentage of their own mass during the disruption. The bottom panels show snapshots of the simulation at two specific times: 0.16 and 4.42 days (shown as vertical lines in the top panel).

respect to \mathbf{J}_{bin} for the disrupting BH and $S_2 \approx 0.136$ at angle 0.14 rad with respect to \mathbf{J}_{bin} for the non-disrupting BH, leading to $\chi_{\text{eff}} \approx -0.019$. The spin angle of the disrupting BH is consistent with the angle with respect to \mathbf{J}_{bin} of the star at the time of the second disruption. The non-disrupting black hole accretes the majority of the mass in the plane of the binary, as in the OS case. We note that the spin angle in these interactions can change due to multiple encounters, as can be clearly seen in Figure 3 for the OS scenario. The low χ_{eff} obtained in this simulation is due to the fact that the spins are anti-aligned in spite of the significant mass accreted. The general behavior expected from these interactions is discussed further in Section 4.1.

4. Discussion

The detection of GW150914 and subsequent LBBH merger GW observations have opened up many questions about LBBH formation history. Individual BH spins within the binary are often used to infer the specific formation channel. In this paper, we have explored the possibility and consequences of an LBBH experiencing a TDE during its lifetime. The accretion that follows from a TDE can possibly spin up each BH and align or anti-align their relative spins. The notion of temporary spin (mis)alignment contrasts with the usual assumption that BH spins are non-evolving and remain unaltered from BH formation to merger. The implications of these tidal interactions are discussed as follows: Section 4.1 explores spin evolution from single and multiple TDEs; and Section 4.2 presents the possible observational signatures produced by these interactions.

4.1. Spin Evolution

4.1.1. Individual Disruptions

Section 2.2 outlines the possible scenarios for LBBH TDEs, while Section 3.3 shows how the spin magnitude and orientation of each scenario change as a result of these interactions. Following the disruption, accretion disks form around either one or both BHs as shown in Figure 5. The angular momentum distribution of material is initially defined by the orbit of the star before disruption, yet the disk orientation can be tilted as the stream is torqued by the binary (Coughlin et al. 2017). The misalignment between \mathbf{J}_{bin} and \mathbf{J}_{disk} is expected to induce a precession of the accretion disk itself (Nixon & King 2016). The binary should, over longer timescales, induce a warped configuration in the disk with a magnitude depending on the local viscosity. If the accretion disks are misaligned with respect to the rotation axis of a Kerr BH, it will be also subject to Lense-Thirring precession (Bardeen & Petterson 1975).

The reader is reminded here that a particular LBBH experiencing a TDE might not necessarily merge and that these interactions are expected to only temporarily alter the spin orientation of the binary. These changes will be more prominent for heavier stars, which might be expected to occur at a higher rate early in the evolution of the cluster. Figure 6 shows the χ_{eff} distribution of an LBBH after one stellar disruption with $M_* \in [0.5 - 10]M_\odot$ from 10^4 Monte Carlo simulations. Current constraints for LIGO BHs suggest that either they have not disrupted a modestly massive star or the spins attained after the disruption are anti-aligned as is the case with the MOS simulation.

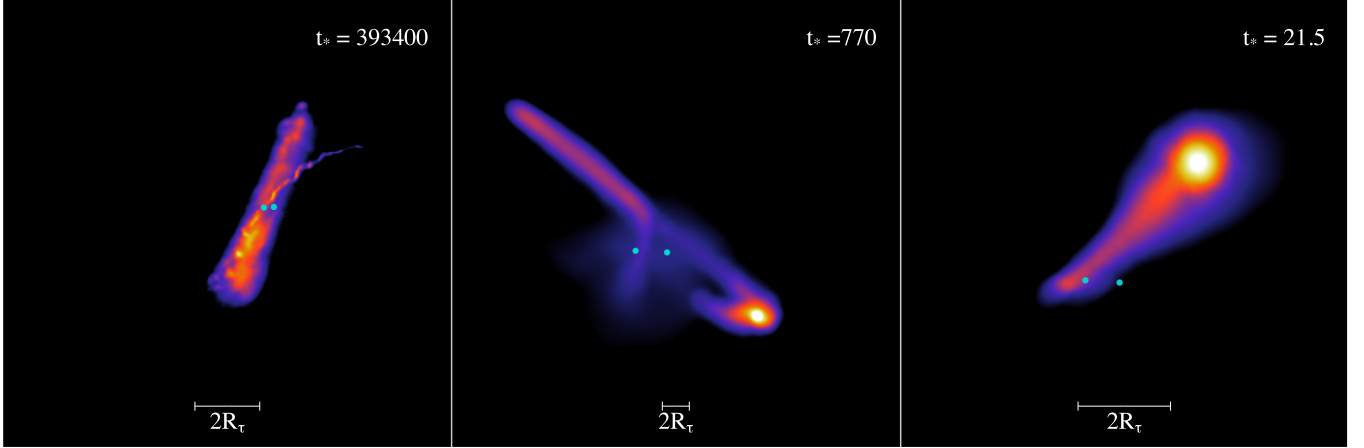


Figure 5. The structure of the accretion disks formed during the circumbinary, overflow, and massive overflow scenarios. Here t_* and R_t denote the time in units of the star's dynamical timescale and the individual tidal radius for each panel, respectively. Left panel: snapshot showing the accretion disk structure at the end of the circumbinary scenario (CS) simulation. The angle of the angular momentum of the disk, \mathbf{J}_{disk} , relative to the orbital angular momentum of the binary, \mathbf{J}_{bin} , is about 2.0 rad. Middle panel: snapshot showing the accretion disk structure after the third TDE (out of a total of four before full disruption) in the overflow scenario (OS). The angle of \mathbf{J}_{disk} relative to \mathbf{J}_{bin} is approximately 0.69 rad. Right panel: snapshot of the accretion disk after the initial TDE in the massive overflow scenario (MOS) case. The angle of \mathbf{J}_{disk} relative to \mathbf{J}_{bin} is ≈ 0.85 rad.

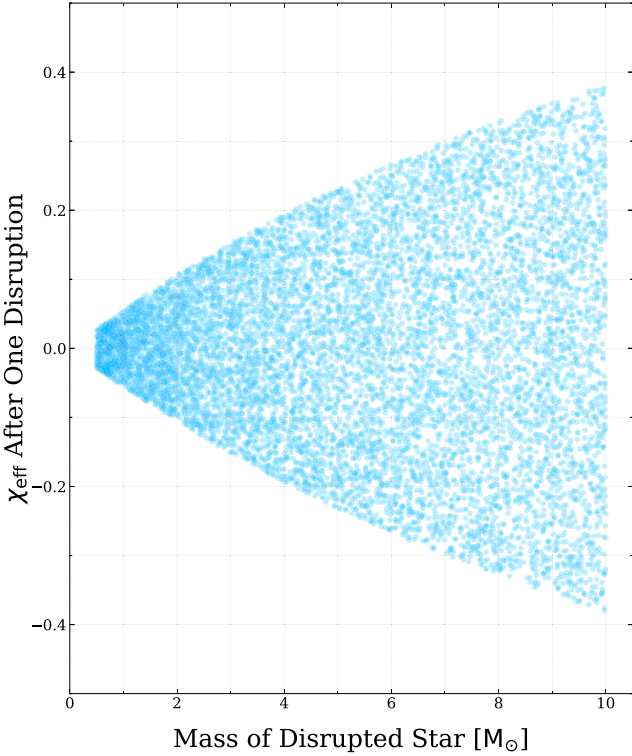


Figure 6. The distribution of χ_{eff} for an LBBH after one tidal disruption of a star with $M_* \in [0.5 - 10] M_\odot$ as derived by 10^4 Monte Carlo simulations assuming a random disruption angle, as shown in Figure 9. As M_* increases χ_{eff} also increases. Therefore, if a BBH LIGO source has small χ_{eff} , then either it has not disrupted a massive star during its lifetime or the resultant high spins are anti-aligned as was the case for us in our MOS simulation.

While TDE interactions will undoubtedly change the spin magnitude of the the accreting BHs, subsequent interactions, expected to take place preferentially with other BHs, will further modify χ_{eff} .

In Section 3.3, we discussed how the accreted spin can go along \mathbf{J}_{bin} or \mathbf{J}_{disk} depending on the particular scenario. The values for the angles we refer to here are specific to the chosen

ICs but, as we argue later, the resultant spin orientations of the BHs generally depend sensitively on \mathbf{J}_{bin} and \mathbf{J}_{disk} .

1. For the SS, the disrupting BH is the only one that accretes significant stellar debris. The accreted spin is observed to be in the direction of \mathbf{J}_{disk} at approximately 1.75 rad, which is set by the angular momentum of the star at the time of disruption.
2. For the CS, the accreted spin of both BHs will be aligned with \mathbf{J}_{disk} . At the time of disruption, \mathbf{J}_{disk} has an angle of about 2.4 rad with respect to \mathbf{J}_{bin} . As the stream of the most bound material returns to pericenter, the binary torques \mathbf{J}_{disk} to an angle of ≈ 2 rad. The torqued stream is responsible for supplying the vast majority of the mass to the disk. As can be seen in the left panel of Figure 5, the initial stream remains in the disruption plane.
3. For the OS, the accreted spin of the disrupting BH is in the direction of \mathbf{J}_{disk} at the time of the initial disruption (at 1.58 rad) while the accreted spin of the non-disrupting BH is aligned with \mathbf{J}_{bin} at an angle of 0.24 rad. The first disruption supplies the disrupting BH with the majority of the accreted mass. The middle panel of Figure 5 shows the disk formed by the third disruption (out of a total of four) whose angle of \mathbf{J}_{disk} is 0.69 rad with respect to \mathbf{J}_{bin} .
4. Contrary to the OS where a single BH is responsible for multiple disruptions, the MOS has disruptions occurring onto both BHs sequentially. Out of the two total disruptions, the second and final disruption contributes the majority of mass accreted by the disrupting BH such that the accreted spin is aligned with \mathbf{J}_{disk} at an angle of 2.2 rad and the non-disrupting BH accretes spin in the direction of \mathbf{J}_{bin} at an angle 0.14 rad. The right panel of Figure 5 shows the disk arising from the first disruption at an angle for \mathbf{J}_{disk} of 0.85 rad with respect to \mathbf{J}_{bin} .
5. For the OS and MOS, where multiple disruptions are possible, the angle of \mathbf{J}_{disk} in Figure 5 is different from the final angular momentum distribution of the disk. This is because the orientation of disk changes after each disruption as a result of the chaotic nature of the three-body dynamics. The disruption resulting in the most

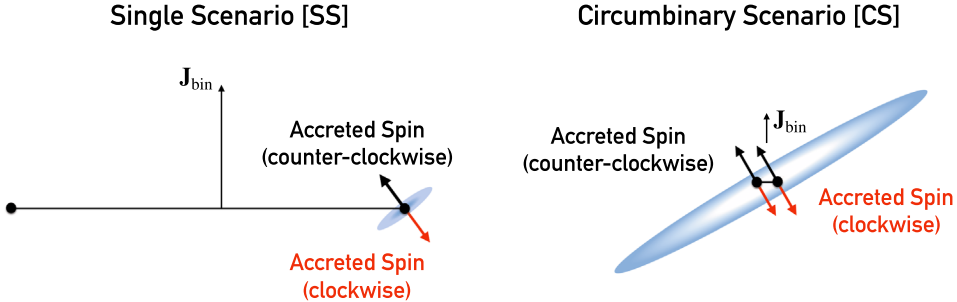


Figure 7. Diagram illustrating how the accreted spin directions of the BHs are set by either J_{disk} or J_{bin} . The black and red arrows show the spin of the BHs expected from accretion of the stellar debris, whose angular momentum distribution can be clockwise or counterclockwise. Left panel: in the SS, a single BH TDE occurs and only the disrupting BH accretes material. The resulting direction of the BH spin is expected to be aligned with the angular momentum of the disk J_{disk} . Right panel: in the CS disruption, a circumbinary disk is formed that allows both BHs to accrete material with similar specific angular momentum.

accretion will nonetheless determine the final orientation of the BH spins.

In general, for a subset of LBBH TDEs, there is a possibility of relative alignment or anti-alignment between the individual BH spins. Alignment or lack thereof is set by the specific conditions of the stellar disruption as well as by the ensuing orbital dynamics of the binary, as shown in Figures 7 and 8. For the SS, the interaction is similar to a single BH TDE and only the disrupting BH accretes material and will, as a result, be spun up. Therefore, there will be no spin alignment between the BHs at the end of the TDE. In this case, the the spin direction of the accreting BH will be aligned with J_{disk} (Figure 7). For the CS, the accretion disk is expected to form outside of the binary such that the spin directions of both accreting BHs will be similar and aligned with J_{disk} (Figure 7). In the OS, accretion onto each BH is more complicated with the possibility of alignment or anti-alignment. In the case of a single passage disruption, the spin of the non-disrupting BH will increase in the direction of J_{bin} as material is accreted. This is because a steep density gradient is encountered by the BH when it enters the disk region, as illustrated in Figure 8.

The *left panel* of Figure 8 shows two cases that produce aligned BH spins:

1. the star is disrupted outside the LBBH in the direction of the orbital motion, and
2. the star is disrupted inside the LBBH moving against the orbital velocity.

The *right panel* of Figure 8 shows two cases that result in anti-alignment:

1. the star is disrupted outside the LBBH moving against the orbital motion, and
2. the star is disrupted inside the LBBH in the direction of the orbital velocity.

We have discussed, in the context of LBBHs, the dynamics and subsequent accretion of stellar debris after a TDE. In all of the scenarios, we expect the direction of the star relative to binary at the moment of disruption to be an essential parameter in determining the resultant BH spins. To this end, we perform a large set of numerical scattering experiments using the N -body code developed by Samsing et al. (2014) in order to study the distribution of relative angles between the star's velocity and the binary orbital velocity upon disruption. The relative

angle distributions are plotted in Figure 9 for a Sun-like star disrupted by a $15M_{\odot}$ equal mass BBH with $e = 0.5$. From the scattering experiments we conclude that there is no preferred distribution and, as such, we predict equal probability for alignment and anti-alignment in the OS. It is expected that LBBHs will experience multiple interactions before merging (e.g., Rodriguez et al. 2016a) and as such, any temporary alignment might be erased before coalescence. TDE interactions from assembly to merge will nevertheless alter the spin magnitudes of the LBBHs. It is then tempting to try to constraint the spin properties of LBBHs experiencing multiple TDEs and it is to this issue that we now turn our attention.

4.1.2. Multiple TDEs and Their Relevance to LBBH Growth

LIGO has uncovered a population of BHs that is more massive than the population known to reside in accreting binaries (Remillard & McClintock 2006). One proposed model for the formation of LIGO BHs is through hierarchical mergers of lighter BHs. In this case, repeated mergers are expected to leave a clear imprint on the spin of the final merger product (Fishbach et al. 2017; Gerosa & Berti 2017; Rodriguez et al. 2018b; Samsing & Ilan 2019). It should be stated, however, that asymmetric GW emission from a merger could eject up to around 30% of merger products from the cluster (Morawski et al. 2018). For LBBHs that do form hierarchically, the distribution of spin magnitudes is universal and weighted toward high spins. Such a distribution appears to be disfavored by current observations. This encourages us to investigate spin distributions emerging from LBBHs accreting from multiple TDEs.

Three sets of simulations are explored here that aim to describe the evolution of LBBHs that undergo multiple TDEs before merging. Each simulation starts with a binary with $M_{\text{bh}_1} = M_{\text{bh}_2} = 15M_{\odot}$ disrupting stars with $M_{\star} = 1M_{\odot}$ ($q = 0.067$). These binaries are assumed to disrupt stars isotropically with respect to J_{bin} . Then for each set of simulations, we change the initial χ_{eff} , which is presumed to be set at BH formation or by the early disruption of a more massive star when the cluster was younger. Figure 10 shows our results. The *top panel* initializes the binary with $\chi_{\text{eff}} = 0$, while the *middle* and *bottom* panels start the binary with $\chi_{\text{eff}} = 0.2$ and $\chi_{\text{eff}} = 0.4$, respectively. For simplicity, we assume the stars are on parabolic orbits and are fully disrupted in one passage. This results in a total mass accreted of about $0.5M_{\star}$ per event, which is modified by an accretion efficiency

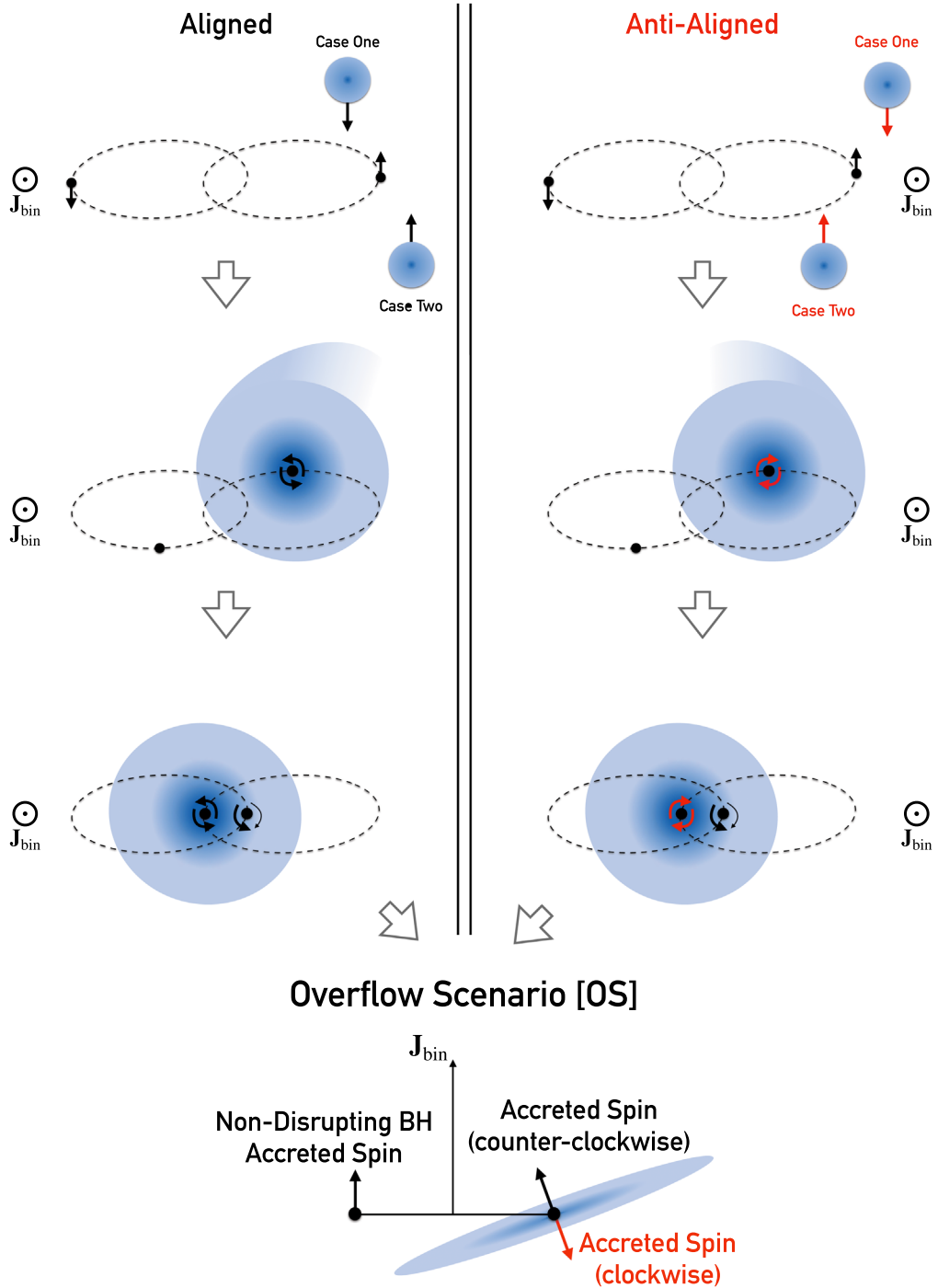


Figure 8. Two cases are depicted that produce aligned BH spins as well as two cases that give rise to anti-aligned BH spins, all of them belonging to the OS. In all cases, the non-disrupting BH accretes spin in the direction of J_{bin} , due to the density gradient it encounters when it enters the accretion disk. The vectors in the left and right panels indicate the velocity while the vectors in the bottom panels indicate the spin angular momentum unless noted otherwise. Left and right panels: a view of the LBBH orbital plane before and after a star is disrupted. In each side panel, two cases are depicted for the star's orbital motion, which determines the orientation of J_{disk} . Bottom panel: a side view of the LBBH with the final accreted spin directions from both the aligned and anti-aligned configurations. The spin of the non-disrupting BH is always oriented in the direction of J_{bin} . The alignment or anti-alignment of the BH spins is thus mainly determined by the motion of the star before it gets disrupted.

that is dependent on the spin of the BH at the time of disruption. This is done in order to account for the radiated energy required for a particle at the innermost stable circular orbit to fall into the BH as described in Bardeen et al. (1972) and Misner et al. (2017). Figure 10 shows that if LIGO sources are built up through TDEs, $|\chi_{\text{eff}}| \lesssim 0.2$ (see also Mandel 2007). Furthermore, we show that an initial χ_{eff} can be significantly

reduced if BH growth in the binary is further promoted by TDEs.

4.2. Observable Signatures

A primary source of interest of TDE interactions has been their prospects as transient sources. These tidal interactions

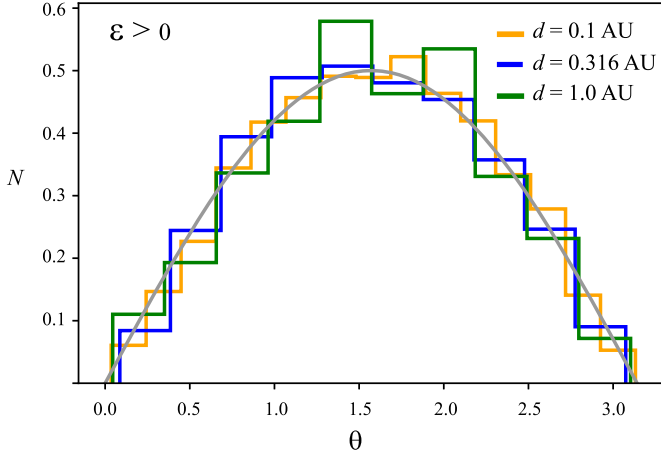


Figure 9. The distributions of relative angles θ between the stellar velocity vector and the binary orbital velocity vector upon disruption. Similar to Figure 1, the orbital trajectories are calculated for a Sun-like star ($M_* = 1M_\odot$, $R_* = R_\odot$) interacting with a $15M_\odot$ equal mass LBBH with $e = 0.5$. The panels show the distribution of θ for different binary separations ($d = 1.0$ au = $87.3R_\tau$, $d = 0.316$ au = $27.6R_\tau$, $d = 0.1$ au = $8.73R_\tau$). The trajectories for bound ($\varepsilon > 0$) and unbound ($\varepsilon < 0$) encounters are plotted separately. For comparison, an isotropic θ distribution is shown (gray curve).

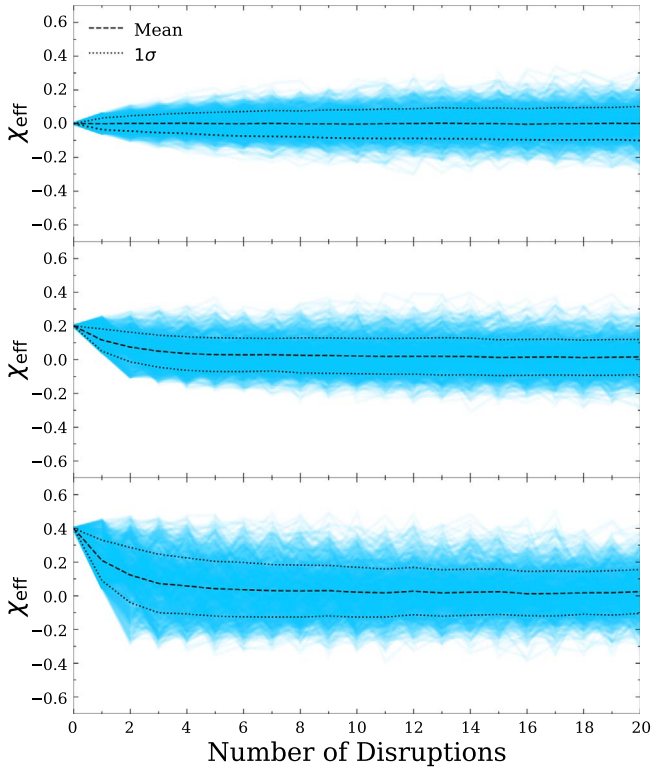


Figure 10. Three sets of simulations are shown, which are aimed at investigating the evolution of LBBHs that undergo multiple TDEs. In all cases, we plot χ_{eff} as a function of the number of disruptions. All simulations start with an LBBH with $M_{\text{bh1}} = M_{\text{bh2}} = 15M_\odot$ disrupting $M_* = 1M_\odot$ stars. The disruptions are assumed to be isotropically distributed. For each case, we change the initial χ_{eff} . The top, middle, and bottom panels start the binary with $\chi_{\text{eff}} = 0$, $\chi_{\text{eff}} = 0.2$, and $\chi_{\text{eff}} = 0.4$, respectively.

feed material to the BH at rates that are orders of magnitude above the Eddington photon limit (Figure 4). The total energy, however, is similar from that of other phenomena encountered in astrophysics, and is in fact reminiscent of that released in gamma-ray bursts (GRBs; Gehrels et al. 2009) and canonical TDE jets (e.g., De Colle et al. 2012). One attractive energy extraction mechanism in these systems, which helps circumvent the Eddington restriction, is the launching of a relativistic

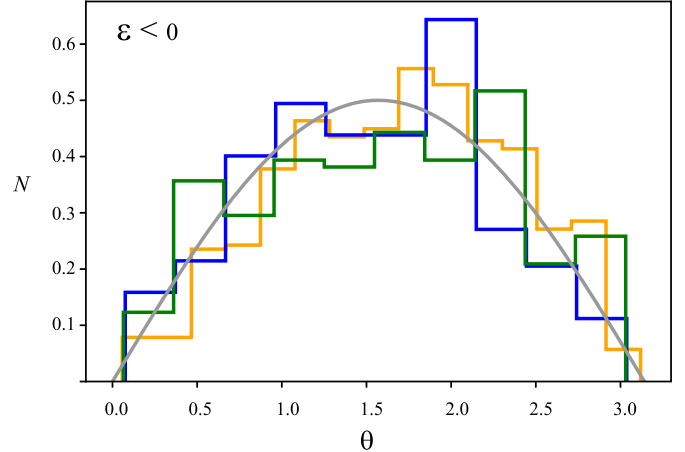


Figure 11. The luminosity and duration of high-energy transients, adapted from Levan et al. (2014). Shown are the predicted luminosities of three of the scenarios for LBBH TDEs discussed in this paper, assuming $L_j \propto \dot{M}$ and a 10% radiative efficiency. For comparison, we plot the observed high-energy properties of GRBs and jetted TDEs. The timescales and durations of LBBH TDEs are well removed from typical long GRBs, but lie between those of the emerging class of ultra-long GRBs and jetted TDEs.

jet (Ramirez-Ruiz & Rosswog 2009; Giannios & Metzger 2011). Such flows are able to carry both bulk kinetic energy and ordered Poynting flux, which allows high-energy radiation to be produced at large distances from the source, where the flow is optically thin (e.g., MacLeod et al. 2014). The corresponding beamed emission offers a promising observational signature of LBBHs due to its expected high luminosity.

Figure 11 shows the predicted luminosities for stars disrupted by LBBHs assuming that the jet power traces the mass supply to the BH: $L_j \propto \dot{M}c^2$. For comparison, we also plot the luminosities and durations of long γ -ray bursts (LGRBs), jetted TDEs from galactic nuclei as well as those from the newly emerging class of ultra-long GRBs: GRB 101225A, GRB 111209A, and GRB 121027A (Levan et al. 2014). These ultra-long GRBs reach peak X-ray luminosities of $\approx 10^{49}$ erg s $^{-1}$ and show nonthermal spectra that is reminiscent of relativistically beamed emission. The derived properties of these LBBH TDEs appear to place them between ultra-long GRBs and jetted TDEs from galactic nuclei. Our ability to classify long duration transients as events emanating from LBBHs or massive BHs in galactic nuclei is likely to remain a challenge. One alternative in the near term is to search at the astrometric positions of these long transients and see whether they coincide with galactic centers.

Another idea is to look for variations in the observed light curve caused by the binary companion, from which one could extract the orbital time of the disrupting BBH and thereby its orbital parameters (e.g., Liu et al. 2014). The relativistically beamed emission from these events is the only component that might be readily detectable since the disk emission is expected to be Eddington limited. We therefore conclude that one avenue for constraining whether or not LBBHs reside in star clusters is searching for their high-energy signatures. The possibility of collecting a sample of such events in coming years with *Swift* appears promising, provided that the rate is similar to the LIGO merger rate of LBBHs (for a detailed discussion on detectability the reader is referred to MacLeod et al. 2014). One challenging aspect for detection would be if the majority of these TDEs take place early in the evolution of clusters (Breen & Heggie 2013; Arca Sedda et al. 2018; Askar et al. 2018). In this case, these high- z events will be too faint to be detected even despite the higher accretion rates expected from the disruption of more massive stars.

To get an estimate on the LBBH TDE rate from the local GC population, we start by computing the rate per GC using $\Gamma_{\text{TDE}} \approx N_{\text{BBH}} \times \eta_s \sigma_{\text{TDE}} v_{\text{dis}}$, where N_{BBH} is the number of BBHs per GC, η_s is the number density of single stars, σ_{TDE} is the TDE cross section, and v_{dis} is the cluster velocity dispersion.

The cross section σ_{TDE} can be written as a product of the binary–single interaction cross section and the probability for an interaction to result in a TDE (e.g., Samsing et al. 2017), i.e., $\sigma_{\text{TDE}} \approx \sigma_{\text{bs}} \times P_{\text{TDE}}$. Assuming the gravitational focusing limit for σ_{bs} and $P_{\text{TDE}} \approx 2R_\tau/a$ one finds,

$$\Gamma_{\text{TDE}}^{\text{gal.}} \approx 10^{-6} \text{ yr}^{-1} \left(\frac{\eta_s}{10^5 \text{ pc}^{-3}} \right) \left(\frac{M_{\text{bh}}}{30 M_\odot} \right)^{4/3} \left(\frac{15 \text{ km s}^{-1}}{v_{\text{dis}}} \right),$$

where this rate is per galaxy (5 LBBHs per GC, and 200 GCs per galaxy) derived for solar type stars ($1M_\odot$, $1R_\odot$) interacting with LBBHs of equal mass. This assumes that the pericenter distance is R_τ and is about one order of magnitude smaller than the LIGO merger rate. This event rate will be further observationally suppressed due to the expected beaming and is likely to also depend sensitively on the evolutionary state of the cluster (Breen & Heggie 2013; Arca Sedda et al. 2018; Askar et al. 2018). Therefore, we expect observations of beamed LBBH TDEs to be lower than the inferred LBBH merger rate. However, if one instead considers stellar tidal disruptions by single BHs in GCs the rate of beamed TDEs is higher by a factor roughly given by the number ratio of single BHs to the number of LBBHs,

$$\Gamma_{\text{TDE}}^{\text{BH}} \approx \Gamma_{\text{TDE}}^{\text{LBBH}} \times \frac{N_{\text{BH}}}{N_{\text{BBH}}},$$

where $\Gamma_{\text{TDE}}^{\text{BH}}$ ($\Gamma_{\text{TDE}}^{\text{LBBH}}$) is the rate from single (binary) BH stellar disruptions. Assuming the fraction of LBBHs to be at the percent level then this leads to the rate of stellar single BH TDEs being $\approx 10^{-4}$ yr $^{-1}$ per galaxy, which is much closer to observable limits. This scenario was recently studied in Perets et al. (2016), and might also be used to constrain the BH population that later forms LBBHs. Furthermore, it may be possible to increase the TDE rate by including events in which a single BH interacts with an existing BH–MS binary since such events may result in similar behavior as some BBH TDE scenarios. However, typically the most massive objects in a

given three-body interaction tend to stay bound, and it is more likely that the MS star would be ejected from the system rather than have resonant interactions that lead to a TDE (Heggie 1975; Hills 1989). Nevertheless, we note that our estimate might be on the optimistic side compared to the rates derived in Perets et al. (2016), but any of these estimates should be taken with caution and more sophisticated N -body methods must be used to explore this further.

Irrespective of current uncertainties, the detection or non-detection of long duration transients from BH and LBBH stellar disruptions should offer strong constraints on the population of LBBHs and the nature of the stellar clusters that host them. In an upcoming paper, we explore what the characteristic LBBH orbital parameters are for different cluster types, as well as what we can learn about the dynamical formation of LBBH GW sources from observing the associated population of BH and LBBH TDEs.

The authors thank the anonymous referee for useful comments and S. Schröder, T. Fragos, B. Mockler, S. I. Mandel, W. Farr, C. Miller, D. J. D’Orazio, K. Hotokezaka, M. Gaspari, and A. Askar for stimulating discussions. M.L.J.R. acknowledges that all praise and thanks belongs to Allah (any benefit is due to God and any shortcomings are my own). E.R.R. acknowledges support from the DNRF (Niels Bohr Professor) and NSF grant AST-1615881. J.S. acknowledges support from the Lyman Spitzer Fellowship. The authors further thank the Niels Bohr Institute for its hospitality while part of this work was completed, and the Kavli Foundation and the DNRF for supporting the 2017 Kavli Summer Program.

Software: GADGET (Springel 2005; Pakmor et al. 2012), SPLASH (Price 2011), Astropy (Astropy Collaboration et al. 2013).

ORCID iDs

- Martin Lopez, Jr. <https://orcid.org/0000-0002-2446-4366>
Aldo Batta <https://orcid.org/0000-0002-3269-3847>
Enrico Ramirez-Ruiz <https://orcid.org/0000-0003-2558-3102>

References

- Abbott, B. P., Abbott, R., Abbott, T. D., et al. 2016, *PhRvL*, 116, 061102
Antonini, F., & Rasio, F. A. 2016, *ApJ*, 831, 187
Arca Sedda, M., Askar, A., & Giersz, M. 2018, *MNRAS*, 479, 4652
Askar, A., Arca Sedda, M., & Giersz, M. 2018, *MNRAS*, 478, 1844
Askar, A., Szkuldrak, M., Gondek-Rosińska, D., Giersz, M., & Bulik, T. 2017, *MNRAS*, 464, L36
Astropy Collaboration, Robitaille, T. P., Tollerud, E. J., et al. 2013, *A&A*, 558, A33
Bardeen, J. M. 1970, *Natur*, 226, 64
Bardeen, J. M., & Petterson, J. A. 1975, *ApJL*, 195, L65
Bardeen, J. M., Press, W. H., & Teukolsky, S. A. 1972, *ApJ*, 178, 347
Bartos, I., Kocsis, B., Haiman, Z., & Márka, S. 2017, *ApJ*, 835, 165
Batta, A., Ramirez-Ruiz, E., & Fryer, C. 2017, *ApJL*, 846, L15
Belczynski, K., Holz, D. E., Bulik, T., & O’Shaughnessy, R. 2016, *Natur*, 534, 512
Bird, S., Cholis, I., Muñoz, J. B., et al. 2016, *PhRvL*, 116, 201301
Bonnerot, C., Rossi, E. M., Lodato, G., & Price, D. J. 2016, *MNRAS*, 455, 2253
Breen, P. G., & Heggie, D. C. 2013, *MNRAS*, 436, 584
Cannizzo, J. K., Lee, H. M., & Goodman, J. 1990, *ApJ*, 351, 38
Carr, B., Kühnel, F., & Sandstad, M. 2016, *PhRvD*, 94, 083504
Cholis, I., Kovetz, E. D., Ali-Haïmoud, Y., et al. 2016, *PhRvD*, 94, 084013
Coughlin, E. R., Armitage, P. J., Nixon, C., & Begelman, M. C. 2017, *MNRAS*, 465, 3840

- De Colle, F., Guillochon, J., Naiman, J., & Ramirez-Ruiz, E. 2012, *ApJ*, **760**, 103
- de Mink, S. E., Cantiello, M., Langer, N., et al. 2009, *A&A*, **497**, 243
- de Mink, S. E., & Mandel, I. 2016, *MNRAS*, **460**, 3545
- Dominik, M., Belczynski, K., Fryer, C., et al. 2012, *ApJ*, **759**, 52
- Dominik, M., Belczynski, K., Fryer, C., et al. 2013, *ApJ*, **779**, 72
- D’Orazio, D. J., & Loeb, A. 2018, *PhRvD*, **97**, 083008
- Downing, J. M. B., Benacquista, M. J., Giersz, M., & Spurzem, R. 2010, *MNRAS*, **407**, 1946
- Downing, J. M. B., Benacquista, M. J., Giersz, M., & Spurzem, R. 2011, *MNRAS*, **416**, 133
- Egginton, P. P. 1983, *ApJ*, **268**, 368
- Evans, C. R., & Kochanek, C. S. 1989, *ApJL*, **346**, L13
- Farr, B., Holz, D. E., & Farr, W. M. 2018, *ApJL*, **854**, L9
- Farr, W. M., Sravan, N., Cantrell, A., et al. 2011, *ApJ*, **741**, 103
- Farr, W. M., Stevenson, S., Miller, M. C., et al. 2017, *Natur*, **548**, 426
- Fishbach, M., Holz, D. E., & Farr, B. 2017, *ApJL*, **840**, L24
- Gehrels, N., Ramirez-Ruiz, E., & Fox, D. B. 2009, *ARA&A*, **47**, 567
- Gerosa, D., & Berti, E. 2017, *PhRvD*, **95**, 124046
- Gezari, S., Heckman, T., Cenko, S. B., et al. 2009, *ApJ*, **698**, 1367
- Giannios, D., & Metzger, B. D. 2011, *MNRAS*, **416**, 2102
- Gondán, L., Kocsis, B., Raffai, P., & Frei, Z. 2018, *ApJ*, **860**, 5
- Guillochon, J., Manukian, H., & Ramirez-Ruiz, E. 2014, *ApJ*, **783**, 23
- Guillochon, J., & Ramirez-Ruiz, E. 2013, *ApJ*, **767**, 25
- Guillochon, J., & Ramirez-Ruiz, E. 2015, *ApJ*, **809**, 166
- Hayasaki, K., Stone, N., & Loeb, A. 2016, *MNRAS*, **461**, 3760
- Heggie, D. C. 1975, *MNRAS*, **173**, 729
- Hills, J. G. 1989, *AJ*, **97**, 222
- Hoang, B.-M., Naoz, S., Kocsis, B., Rasio, F. A., & Dosopoulou, F. 2018, *ApJ*, **856**, 140
- Hong, J., & Lee, H. M. 2015, *MNRAS*, **448**, 754
- Iben, I., Jr., & Livio, M. 1993, *PASP*, **105**, 1373
- Ivanova, N., Justham, S., Chen, X., et al. 2013, *A&ARv*, **21**, 59
- Janiuk, A., Bejger, M., Charzyński, S., & Sukova, P. 2017, *NewA*, **51**, 7
- Kalogera, V. 2000, *ApJ*, **541**, 319
- Kalogera, V., Belczynski, K., Kim, C., O’Shaughnessy, R., & Willem, B. 2007, *PhR*, **442**, 75
- Kocsis, B., & Levin, J. 2012, *PhRvD*, **85**, 123005
- Kremer, K., Chatterjee, S., Ye, C. S., Rodriguez, C. L., & Rasio, F. A. 2019, *ApJ*, **871**, 38
- Kroupa, P., Weidner, C., Pflamm-Altenburg, J., et al. 2013, in The Stellar and Sub-Stellar Initial Mass Function of Simple and Composite Populations, ed. T. D. Oswalt & G. Gilmore (Dordrecht: Springer), 115
- Levan, A. J., Tanvir, N. R., Starling, R. L. C., et al. 2014, *ApJ*, **781**, 13
- Liu, F. K., Li, S., & Komossa, S. 2014, *ApJ*, **786**, 103
- Lodato, G., & Rossi, E. M. 2011, *MNRAS*, **410**, 359
- Loeb, A. 2016, *ApJL*, **819**, L21
- MacLeod, M., Goldstein, J., Ramirez-Ruiz, E., Guillochon, J., & Samsing, J. 2014, *ApJ*, **794**, 9
- Mandel, I. 2007, arXiv:0707.0711
- Mandel, I., & de Mink, S. E. 2016, *MNRAS*, **458**, 2634
- Marchant, P., Langer, N., Podsiadlowski, P., Tauris, T. M., & Moriya, T. J. 2016, *A&A*, **588**, A50
- McKernan, B., Ford, K. E. S., Bellovary, J., et al. 2018, *ApJ*, **866**, 66
- Misner, C. W., Thorne, K. S., & Wheeler, J. A. 2017, Gravitation (Princeton, NJ: Princeton Univ. Press)
- Mockler, B., Guillochon, J., & Ramirez-Ruiz, E. 2019, *ApJ*, **872**, 151
- Morawski, J., Giersz, M., Askar, A., & Belczynski, K. 2018, *MNRAS*, **481**, 2168
- Nixon, C., & King, A. 2016, in Lecture Notes in Physics, ed. F. Haardt et al., Vol. 905 (Berlin: Springer), 45
- O’Leary, R. M., Kocsis, B., & Loeb, A. 2009, *MNRAS*, **395**, 2127
- O’Leary, R. M., Meiron, Y., & Kocsis, B. 2016, *ApJL*, **824**, L12
- Paczynski, B. 1976, in IAU Symp. 73, Structure and Evolution of Close Binary Systems, ed. P. Eggleton, S. Mitton, & J. Whelan (Dordrecht: Reidel), 75
- Pakmor, R., Edelmann, P., Röpke, F. K., & Hillebrandt, W. 2012, *MNRAS*, **424**, 2222
- Perets, H. B., Li, Z., Lombardi, J. C., Jr., & Milcarek, S. R., Jr. 2016, *ApJ*, **823**, 113
- Phinney, E. S. 1989, in IAU Symp. 136, The Center of the Galaxy, ed. M. Morris (Dordrecht: Kluwer), 543
- Podsiadlowski, P. 2001, in ASP Conf. Ser. 229, Evolution of Binary and Multiple Star Systems, ed. P. Podsiadlowski et al. (San Francisco, CA: ASP), 239
- Portegies Zwart, S. F., & McMillan, S. L. W. 2000, *ApJL*, **528**, L17
- Postnov, K. A., & Yungelson, L. R. 2014, *LRR*, **17**, 3
- Price, D. J. 2011, SPLASH: An Interactive Visualization Tool for Smoothed Particle Hydrodynamics Simulations, arXiv:1103.004
- Ramirez-Ruiz, E., & Rosswog, S. 2009, *ApJL*, **697**, L77
- Rees, M. J. 1988, *Natur*, **333**, 523
- Remillard, R. A., & McClintock, J. E. 2006, *ARA&A*, **44**, 49
- Rodriguez, C. L., Amaro-Seoane, P., Chatterjee, S., et al. 2018a, *PhRvD*, **98**, 123005
- Rodriguez, C. L., Amaro-Seoane, P., Chatterjee, S., & Rasio, F. A. 2018b, *PhRvL*, **120**, 151101
- Rodriguez, C. L., Chatterjee, S., & Rasio, F. A. 2016a, *PhRvD*, **93**, 084029
- Rodriguez, C. L., Haster, C.-J., Chatterjee, S., Kalogera, V., & Rasio, F. A. 2016b, *ApJL*, **824**, L8
- Rodriguez, C. L., Morscher, M., Pattabiraman, B., et al. 2015, *PhRvL*, **115**, 051101
- Rodriguez, C. L., Zevin, M., Pankow, C., Kalogera, V., & Rasio, F. A. 2016c, *ApJL*, **832**, L2
- Samsing, J. 2018, *PhRvD*, **97**, 103014
- Samsing, J., Askar, A., & Giersz, M. 2018a, *ApJ*, **855**, 124
- Samsing, J., & D’Orazio, D. J. 2018, *MNRAS*, arXiv:1804.06519
- Samsing, J., & Ilan, T. 2018, *MNRAS*, **476**, 1548
- Samsing, J., & Ilan, T. 2019, *MNRAS*, **482**, 30
- Samsing, J., MacLeod, M., & Ramirez-Ruiz, E. 2014, *ApJ*, **784**, 71
- Samsing, J., MacLeod, M., & Ramirez-Ruiz, E. 2017, *ApJ*, **846**, 36
- Samsing, J., MacLeod, M., & Ramirez-Ruiz, E. 2018b, *ApJ*, **853**, 140
- Samsing, J., & Ramirez-Ruiz, E. 2017, *ApJL*, **840**, L14
- Sasaki, M., Suyama, T., Tanaka, T., & Yokoyama, S. 2016, *PhRvL*, **117**, 061101
- Schröder, S. L., Batta, A., & Ramirez-Ruiz, E. 2018, *ApJL*, **862**, L3
- Shikawa, H., Krolik, J. H., Cheng, R. M., Piran, T., & Noble, S. C. 2015, *ApJ*, **804**, 85
- Sigurdsson, S., & Hernquist, L. 1993, *Natur*, **364**, 423
- Springel, V. 2005, *MNRAS*, **364**, 1105
- Stephan, A. P., Naoz, S., Ghez, A. M., et al. 2016, *MNRAS*, **460**, 3494
- Stone, N. C., Metzger, B. D., & Haiman, Z. 2017, *MNRAS*, **464**, 946
- Strubbe, L. E., & Quataert, E. 2011, *MNRAS*, **415**, 168
- Taan, R. E., & Ricker, P. M. 2010, *NewAR*, **54**, 65
- The LIGO Scientific Collaboration & The Virgo Collaboration 2018, arXiv:1811.12907
- Ulmer, A. 1998, in AIP Conf. Ser. 431, The Tidal Disruption of Stars By Massive Black Holes, ed. S. S. Holt & T. R. Kallman (Melville, NY: AIP), 141
- VanLandingham, J. H., Miller, M. C., Hamilton, D. P., & Richardson, D. C. 2016, *ApJ*, **828**, 77
- Voss, R., & Tauris, T. M. 2003, *MNRAS*, **342**, 1169
- Woosley, S. E. 2016, *ApJL*, **824**, L10
- Zevin, M., Pankow, C., Rodriguez, C. L., et al. 2017, *ApJ*, **846**, 82
- Zevin, M., Samsing, J., Rodriguez, C., Haster, C.-J., & Ramirez-Ruiz, E. 2019, *ApJ*, **871**, 91
- Ziosi, B. M., Mapelli, M., Branchesi, M., & Tormen, G. 2014, *MNRAS*, **441**, 3703